Magn Reson Med Sci 2021; 20; 47–59
doi:10.2463/mrms.mp.2019-0193
Published Online: February 27, 2020

MAJOR PAPER

Optimal Combination of Features on Gadoxetate Disodium-enhanced MR Imaging for Non-invasive Differential Diagnosis of Hepatocellular Carcinoma: The JAMP-HCC Study

Shintaro Ichikawa[1], Utaroh Motosugi[1*], Hiroyuki Morisaka[2], Kazuto Kozaka[3], Satoshi Goshima[4,5], and Tomoaki Ichikawa[2]

Purpose: To determine the optimal combination of gadoxetate disodium-enhanced magnetic resonance imaging (MRI) findings for the diagnosis of hepatocellular carcinoma (HCC) and to compare its diagnostic ability to that of dynamic computed tomography (CT) in patients with chronic liver disease.

Methods: This multi-institutional study consisted of two parts: Study 1, a retrospective study to determine the optimal combination of gadoxetate disodium-enhanced MRI findings (decision tree and logistic model) to distinguish HCC (n = 199) from benign (n = 81) or other malignant lesions (n = 95) (375 nodules in 269 patients) and Study 2, a prospective study to compare the diagnostic ability of gadoxetate disodium-enhanced MRI to distinguish HCC (n = 73) from benign (n = 15) or other malignant lesions (n = 12) with that of dynamic CT (100 nodules in 83 patients). Two radiologists independently evaluated the imaging findings (Study 1 and 2) and made a practical diagnosis (Study 2).

Results: In Study 1, rim or whole enhancement on arterial phase images, signal intensities on T_2-weighted/diffusion-weighted/portal venous/transitional/hepatobiliary phase images, and signal drop on opposed-phase images were independently useful for differential diagnosis. In Study 2, the accuracy, sensitivity, negative predictive value, and negative likelihood ratio of the CT decision tree (reader 2) were higher than those of MRI Model 2 (P = 0.015–0.033). There were no other significant differences in diagnostic ability (P = 0.059–1.000) and radiologist-made practical diagnosis (P = 0.059–1.000) between gadoxetate disodium-enhanced MRI and CT.

Conclusion: We identified the optimal combination of gadoxetate disodium-enhanced MRI findings for HCC diagnosis. However, its diagnostic ability was not superior to that of dynamic CT.

Keywords: *hepatocellular carcinoma, magnetic resonance imaging, decision trees, logistic models, gadoxetate disodium*

[1]Department of Radiology, University of Yamanashi, Yamanashi, Japan
[2]Department of Diagnostic Radiology, Saitama Medical University International Medical Center, Saitama, Japan
[3]Department of Radiology, Kanazawa University Graduate School of Medical Sciences, Ishikawa, Japan
[4]Department of Diagnostic Radiology and Nuclear Medicine, Hamamatsu University School of Medicine, Shizuoka, Japan
[5]Department of Radiology, Gifu University, Gifu, Japan

[*]Corresponding author: Department of Radiology, University of Yamanashi, 1110 Shimokato, Chuo-shi, Yamanashi, 409-3898, Japan. Phone: +81-55-273-1111, Fax: +81-55-273-6744, E-mail: umotosugi@nifty.com

Received: December 11, 2019 | Accepted: January 28, 2020

Introduction

Liver cancer is the third leading cause of cancer-related deaths, contributing to 781,000 deaths yearly worldwide.[1] Hepatocellular carcinoma (HCC) is the predominant primary liver cancer in many countries, and HCC-related mortality continues to increase.[2–4] The computed tomography (CT) and magnetic resonance imaging (MRI) characteristics of HCC are well described, and the diagnostic algorithm for HCC [Liver reporting and data system (LI-RADS)], which is based on CT, MRI with extracellular contrast material, or MRI with hepatobiliary contrast material (namely, gadoxetate disodium, also known by the trade name Primovist or Eovist), has been established.[5,6]

Gadoxetate disodium is a liver-specific contrast material that allows both dynamic study and hepatocyte imaging at the hepatobiliary phase (HBP). Currently, gadoxetate disodium is widely used for liver MRI in daily clinical practice because of its high performance for lesion detection and characterization.[7–9] Gadoxetate disodium-enhanced MRI has a better diagnostic ability than that of CT for HCC in patients with cirrhosis, particularly those with small lesions.[10–12] However, gadoxetate disodium-enhanced MRI also has some pitfalls. The image quality at the arterial phase (AP) may be insufficient due to transient dyspnea,[13,14] inappropriate scanning time, or truncation artifact caused by low injection volume of gadoxetate disodium.[15] It is often difficult to detect an enhancing capsule at the portal venous phase (PVP) or transitional phase (TP) of gadoxetate disodium-enhanced MRI[16] because of high enhancement of the adjacent parenchyma on PVP or TP. HBP hypointensity is an ancillary feature that may indicate the presence of malignancy according to the LI-RADS. Although this finding is characteristic of HCC, it is not specific for HCC. Moreover, approximately 10–20% of progressed HCCs show hyperintensity on HBP.[17,18] Therefore, we hypothesized that it is necessary to combine several imaging findings on gadoxetate disodium-enhanced MRI to correctly diagnose HCC.

The purpose of this study was to determine the optimal combination of gadoxetate disodium-enhanced MRI findings for the diagnosis of HCC and to compare the diagnostic ability of gadoxetate disodium-enhanced MRI to that of dynamic CT in patients with chronic liver disease.

Materials and Methods

Study design

This multi-institutional study consisted of two parts: Study 1, a retrospective study to determine the optimal combination of gadoxetate disodium-enhanced MRI findings to distinguish HCC from benign or other malignant lesions and construct a decision tree and logistic model for the diagnosis of HCC; and Study 2, a prospective study to compare the diagnostic ability of gadoxetate disodium-enhanced MRI to distinguish HCC from other lesions with that of dynamic CT (Fig. 1). The trial protocol was approved by a Central Ethics Committee and local Institutional Review Boards of 12 participating institutions. For Study 1, the requirement for written informed consent was waived because of the retrospective nature of the study. For Study 2, all patients gave their informed written consent before enrollment.

Patient enrollment

Study 1

Patients were consecutively enrolled from 12 hospitals between July 2008 and October 2014. The inclusion criteria were as follows: (i) available gadoxetate disodium-enhanced MRI data, (ii) pathologically confirmed HCC or other malignant lesions, and (iii) presence of chronic liver disease. Clinically diagnosed benign lesions and an HBP hypointense nodule without arterial phase hyperenhancement (APHE),[19] whose size did not increase during an observation period of >1 year, were also included.

Study 2

Patients were consecutively enrolled from 12 hospitals between August 2013 and February 2016. The inclusion criteria were as follows: (i) planned gadoxetate disodium-enhanced MRI and CT within 2 months due to suspicion of liver lesions and (ii) presence of chronic liver disease. Clinically diagnosed benign lesions and an HBP hypointense nodule without APHE, whose size did not increase on MRI/CT during an observation period >2 years, were included.

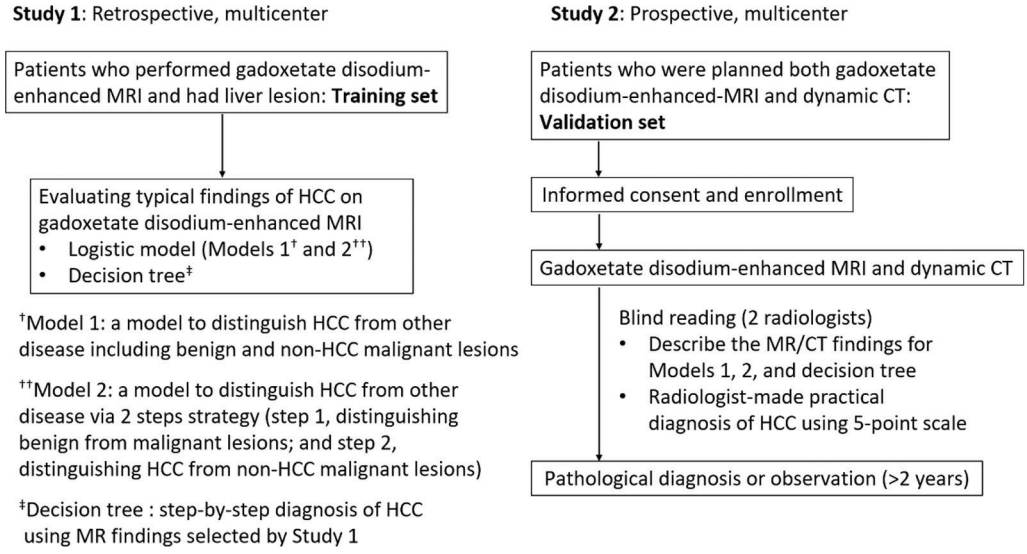

Fig. 1 Flowchart of the study design. HCC, hepatocellular carcinoma; CT, computed tomography; MRI, magnetic resonance imaging.

A pathological diagnosis was required for HCC and other malignant lesions.

MRI and CT protocols

Gadoxetate disodium-enhanced MRI was performed using a superconducting magnet scanner operated at 1.5T or 3T. Gadoxetate disodium (0.025 mmol/kg body weight) was administered by using a power injector. Required sequences were as follows: T_2-weighted image (T_2WI), gradient-echo dual-phase T_1-weighted image (T_1WI), diffusion-weighted image (DWI), and dynamic study (AP, PVP, TP, and HBP). CT was performed using 64–320-detector-row CT units. Iodine contrast materials (300–370 mg/mL) were administered using a power injector. Four phases (pre-contrast, AP, PVP, and delayed phase) of dynamic study was required. The MRI and CT parameters varied depending on the clinical protocol of each hospital (Table 1) because the imaging studies were performed as part of each hospital's daily practice.

Image analysis

In Study 1, gadoxetate disodium-enhanced MRI was assessed independently by two board-certificated radiologists (T.I. and H.M.) with 30 and 10 years of experience in liver imaging, respectively. They evaluated the imaging findings of target lesions in order to choose one characteristic in each sequence as follows: T_2WI: marked hyperintensity, hyperintensity, isointensity, or hypointensity; gradient-echo T_1WI: presence or absence of signal drop on opposed phase; DWI: hyperintensity, isointensity, or hypointensity; AP: no, dot-like, rim, part, or whole APHE; PVP: marked hypointensity, hypointensity, isointensity or hyperintensity; TP: marked hypointensity, hypointensity, isointensity or hyperintensity; and HBP: no uptake, part and moderate uptake, part and marked uptake, whole and moderate uptake, or wole and marked uptake of gadoxetate disodium (Fig. 2). Any discrepancy between the two readers were resolved by a third board-certificated radiologist (S.I.) with 10 years of experience in liver imaging. In Study 2, gadoxetate disodium-enhanced MRI and CT were assessed independently by two board-certificated radiologists (S.G. and K.K.), both with 17 years of experience in liver imaging. They evaluated MRI findings as in Study 1. For CT, they evaluated whether non-rim APHE and non-peripheral washout were present or not. Radiologist-made practical diagnosis of HCC was also performed for both gadoxetate disodium-enhanced MRI and CT using a 5-point scale of the confidence for the diagnosis of malignancy as well as of HCC (1, definitely benign or non-HCC; 2, probably benign or non-HCC; 3, intermediate probability of malignancy or HCC; 4, probably malignant or HCC; and 5, definitely malignant or HCC). All radiologists were aware that the patients had chronic liver diseases but were unaware of the imaging findings and the final diagnosis.

Table 1 Parameters of MRI and CT

Parameter	Setting
MRI	
T_2-weighted image with or without fat-saturated	
Repetition time/echo time (ms)	2000–20000/66.56–99.94
Matrix	144–384 × 160–356
Field of view (cm)	30–40 × 22–47
Section thickness/intersection gap (mm)	4–8/1–10
Flip angle (°)	90–170
T_1-weighted gradient-echo image	
Repetition time/echo time (ms)	4.28–280/1.12–5.80
Matrix	173–384 × 136–256
Field of view (cm)	32–42 × 27–45
Section thickness/intersection gap (mm)	3–8/0–10
Flip angle (°)	12–80
Diffusion-weighted image	
Repetition time/echo time (ms)	1200–12000/49.9–82
Matrix	72–160 × 72–192
Field of view (cm)	35–45 × 22–47
Section thickness/intersection gap (mm)	5–8/0–10
Flip angle (°)	90
b-Value (s/mm^2)	800–1000
Dynamic study	
Repetition time/echo time (ms)	2.52–5.90/1.08–2.10
Matrix	154–320 × 160–288
Field of view (cm)	30–40 × 27–47
Section thickness/intersection gap (mm)	2.5–8/0–3
Flip angle (°)	10–15
Hepatobiliary phase	
Repetition time/echo time (ms)	2.92–7.89/1.23–2.12
Matrix	154–384 × 160–288
Field of view (cm)	30–42 × 27–47
Section thickness/intersection gap (mm)	2.5–8/0–3
Flip angle (°)	10–20
Scan delay after injection (min)	15–20
CT	
Detector row number	64–320
Section thickness (mm)	1–5
Helical pitch	0.5–1.375
Field of view	28–35
Iodine dose (mgI/kg)	500–600
Injection rate (mL/s)	2–4

MRI, magnetic resonance imaging; CT, computed tomography.

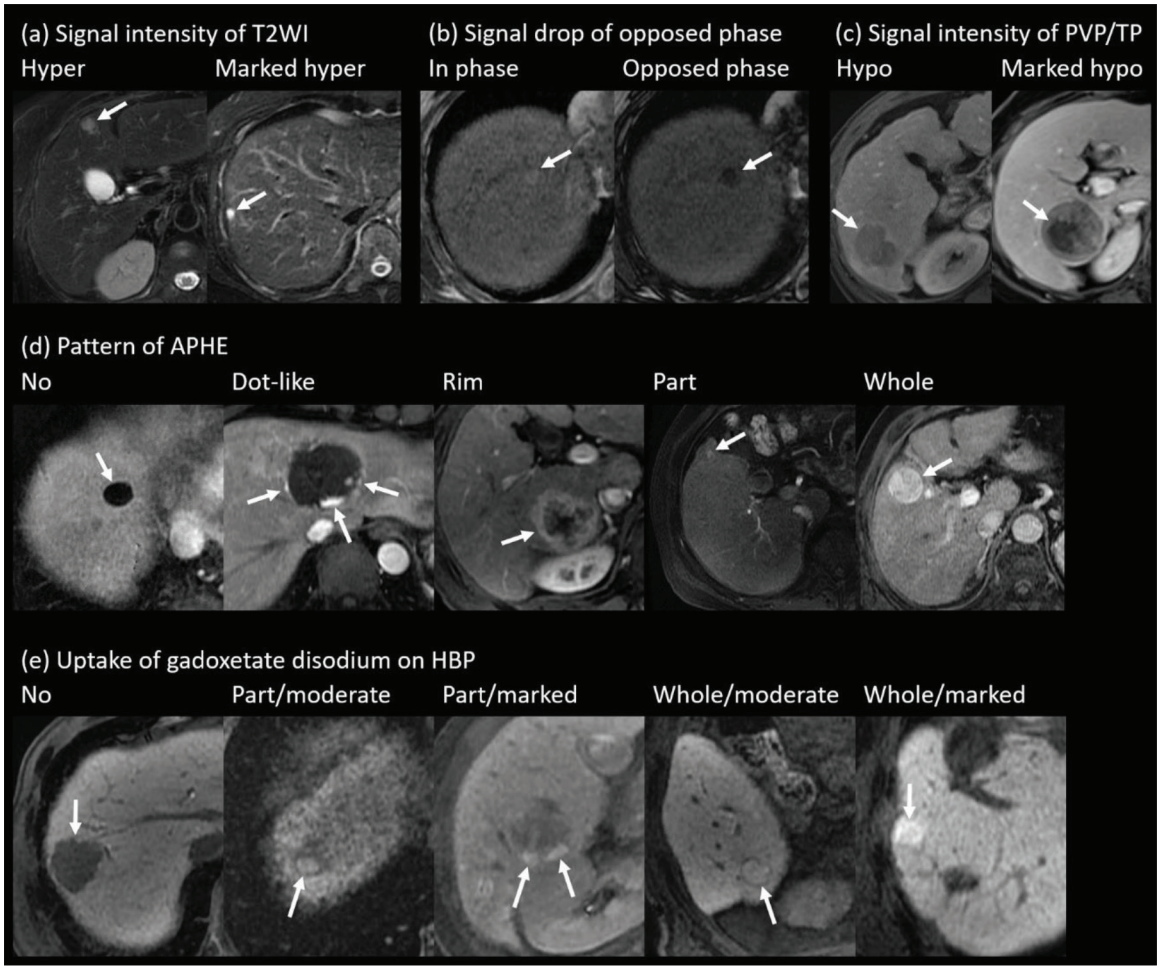

Fig. 2 Examples of magnetic resonance images with visual assessment (only item-specific annotation was needed). (**a**) Signal intensity of T_2-weighted images (T_2WI), (**b**) signal drop of opposed phase, (**c**) signal intensity of the portal venous phase (PVP) or transitional phase (TP), (**d**) pattern of arterial phase hyperenhancement (APHE), and (**e**) uptake of gadoxetate disodium at the hepatobiliary phase (HBP). All images were obtained in the axial plane. (**a**) On T_2WI, hyperintensity was higher than that of the surrounding liver but lower than that of water (arrow), while marked hyperintensity was similar to that of water (arrow). (**b**) Signal drop of opposed phase was defined as a signal of opposed phase lower than in phase signal (arrow). (**c**) On PVP or TP, hypointensity was lower than that of the surrounding liver but higher than that of water (arrow), while marked hypointensity was similar to that of water (arrow). (**d**) Pattern of APHE was divided into five categories: no APHE, whole hypointensity on the arterial phase (arrow); dot-like APHE, peripheral slightly marked nodular enhancement (arrows); rim APHE, peripheral layer enhancement (arrow); part APHE, partially higher intensity than in the surrounding liver (arrow); whole APHE, overall higher intensity than in the surrounding liver (arrow). (**e**) On HBP, pattern of gadoxetate disodium uptake was divided into five categories: no uptake, overall hypointensity (arrow); part and moderate uptake, partially moderate hyperintensity (similar intensity compared with that of the surrounding liver) (arrow); part and marked uptake, partially marked hyperintensity (higher intensity compared with surrounding liver) (arrows); whole and moderate uptake, overall moderate hyperintensity (arrow); whole and marked uptake, overall marked hyperintensity (arrow).

Statistical analysis

Typical findings of HCC on gadoxetate disodium-enhanced MRI were evaluated by logistic regression analysis to generate a logistic model in Study 1 (secondary endpoint). Two types of models were generated: Model 1 was intended to directly distinguish HCCs from other disease including benign and non-HCC malignant lesions; Model 2 was intended to make a diagnosis in line with the LI-RADS guidelines,[5] that is, using a two-step strategy [step 1, distinguishing benign (LR1 and LR2) from malignant lesions; and step 2, distinguishing HCC from non-HCC malignant lesions]. In Study 2, the diagnostic ability of the two logistic models was determined, and the decision tree based on gadoxetate disodium-enhanced MRI to distinguish HCC from other lesions was validated and compared with a CT decision tree (Fig. 3a) (primary endpoint). The CT decision tree was defined on the basis of the classical diagnostic method consisting of non-rim APHE and non-peripheral washout.[20] The ability of a radiologist-made practical diagnosis was compared between CT and MRI.

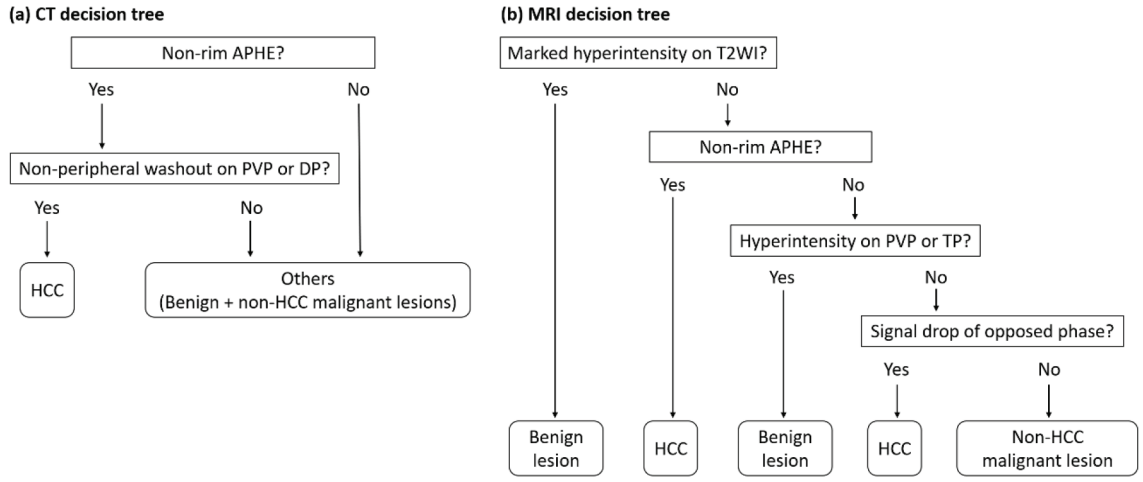

Fig. 3 Decision tree for distinguishing hepatocellular carcinoma from other lesions. (**a**) The computed tomography (CT) decision tree was defined based on the classic diagnostic method consisting of non-rim arterial phase hyperenhancement (APHE) and non-peripheral washout at the portal venous phase (PVP) or delayed phase (DP). (**b**) The magnetic resonance imaging (MRI) decision tree was generated based on the classification and regression tree algorithm in Study 1. HCC, hepatocellular carcinoma; T_2WI, T2-weighted image; TP, transitional phase.

The weighted kappa coefficient was calculated to assess interobserver agreement. Agreement was considered excellent for kappa values (κ) > 0.8, good for $0.6 < \kappa \leq 0.8$, moderate for $0.4 < \kappa \leq 0.6$, fair for $0.2 < \kappa \leq 0.4$, and poor for $\kappa \leq 0.2$. All statistical analyses were performed by professional statisticians outside of this study committee using R (version 3.4.3; The R Foundation for Statistical Computing, Vienna, Austria) and IBM SPSS (version 23.0.0.0; IBM Corporation, Armonk, NY, USA). *P*-values <0.05 were considered statistically significant.

Results

Study 1

Of the 273 patients (382 lesions) initially enrolled in Study 1, four patients (7 lesions) were excluded (Fig. 4). Therefore, the final cohort consisted of 269 patients (198 men and 71 women; mean age, 67.4 ± 10.0 [range, 32–89] years) with 375 liver lesions. The underlying liver diseases of the 269 patients and final diagnoses of the 375 lesions were shown in Fig. 4. The mean size of liver lesions was as follows: HCC, 30.2 ± 24.3 [range, 3–167] mm; benign lesions, 13.2 ± 8.9 [3–56] mm; non-HCC malignant lesions including premalignant lesions, 22.5 ± 17.0 [4–80] mm. The mean time interval between gadoxetate disodium-enhanced MRI and pathological diagnosis was 56.5 ± 81.5 days in HCC and 48.3 ± 40.8 days in other lesions. All the images were evaluable for the blind reading.

Useful findings for distinguishing HCC from benign or non-HCC malignant lesions (Model 1) included signal intensities on T_2WI and PVP/TP images as well as pattern of APHE (all $P < 0.001$). Signal intensity on T_2WI showed the highest partial regression coefficient (2.0302–2.2667) (Table 2). In step 1 of Model 2, useful findings for distinguishing benign lesions from malignant lesions (HCC and non-HCC malignant lesions) included lesion size, signal intensities of T_2WI, DWI and HBP images as well as pattern of APHE (all $P \leq 0.001$). Signal intensities of T_2WI, DWI and HBP images and pattern of APHE showed high partial regression coefficient (3.4136–5.2645) (Table 3). In step 2 of Model 2, useful findings for distinguishing HCC from non-HCC malignant lesions included signal intensity on T_2WI, PVP, and TP images as well as pattern of APHE and signal drop on opposed-phase gradient-echo T_1WI ($P < 0.001$–0.046). Signal intensity on T_2WI and pattern of APHE showed high partial regression coefficient (2.1234–3.9804) (Table 3). The probability of the lesion being HCC or benign was calculated by substituting α into the equation shown in Appendix. If the probability was greater than or equal to the cut-off value calculated from receiver operating characteristic analysis, the lesion was considered HCC or benign. Model 1 had a tendency of higher sensitivity compared with Model 2 (0.879 vs. 0.804), while Model 2 tended to have higher specificity compared with Model 1 (0.881 vs. 0.784) (Table 4). However, Models 1 and 2 showed similar accuracy for distinguishing HCC from others (0.835 vs. 0.840) (Table 4). The diagnostic ability for distinguishing benign lesions from malignant lesions tended to be better than that for distinguishing HCC from non-HCC malignant lesions (Table 5). An MRI decision tree for distinguishing HCC from other lesions was generated through classification and the regression tree algorithm[21] (Fig. 3b).

Study 2

Of the 144 patients (203 lesions) enrolled in Study 2, 61 patients (103 lesions) were excluded (Fig. 4). Therefore, the final cohort consisted of 83 patients (60 men and 23 women; mean age, 70.0 ± 8.6 [range, 33–85] years) with 100 liver lesions. The underlying liver diseases of the 83 patients and final diagnoses of the 100 lesions were shown in Fig. 4. The mean size of liver lesions was as follows: HCC, 36.4 ± 34.9

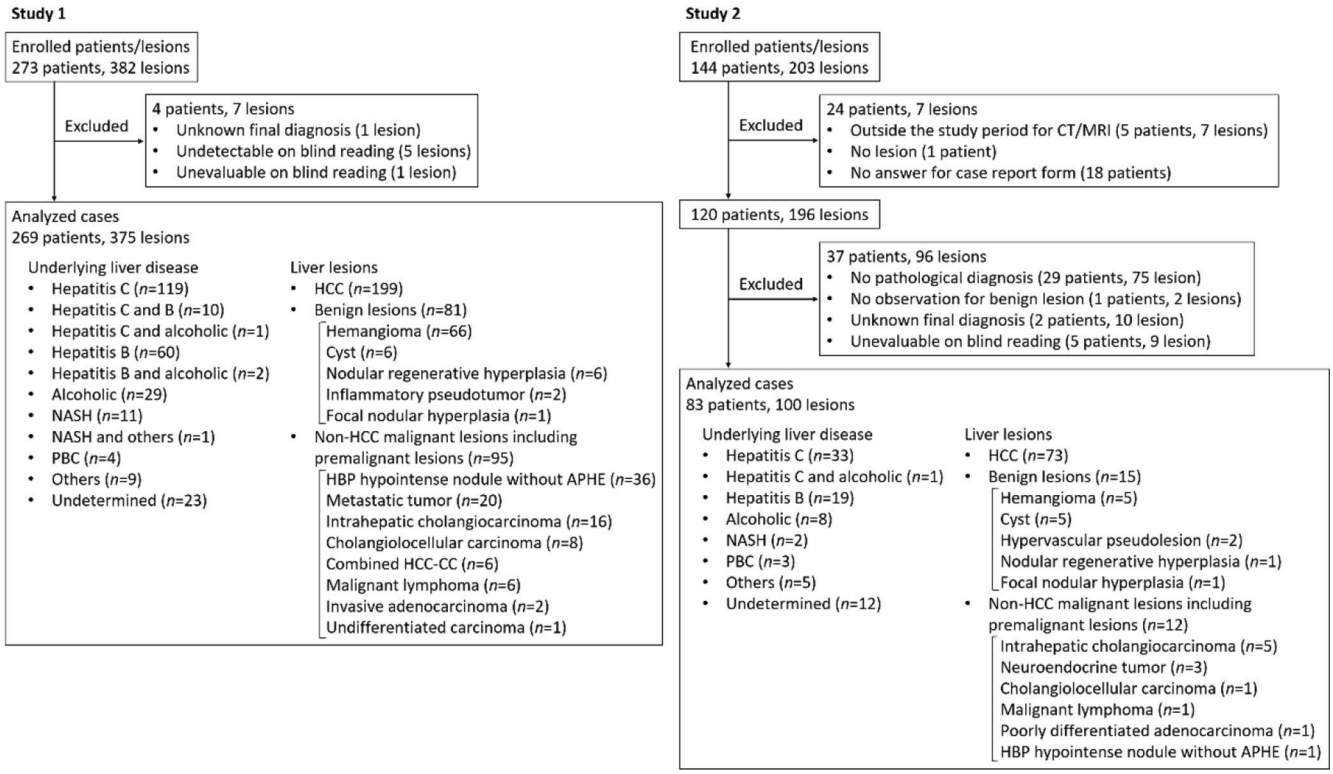

Fig. 4 Flowchart of patient enrollment in Studies 1 and 2. NASH, nonalcoholic steatohepatitis; PBC, primary biliary cholangitis; HCC, hepatocellular carcinoma; HBP, hepatobiliary phase; APHE, arterial phase hyperenhancement; CC, cholangiocarcinoma.

Table 2 Multivariate logistic model of Model 1 in Study 1

	Partial regression coefficient	Odds ratio (95% confidence interval)	*P*-value
HCC (1) vs. others (0) [benign and non-HCC malignant lesions]			
(Constant)	−3.9855	–	–
Size	0.0197	1.02 (1.00–1.04)	0.056
T_2WI			
Marked hyperintensity		Reference category	
Hyperintensity	2.2667	9.65 (3.42–27.22)	<0.001*
Isointensity	2.0302	7.62 (2.56–22.67)	<0.001*
Hypointensity	−13.4752	0.00 (0.00–Inf)	0.984
APHE			
No		Reference category	
Dot-like	−1.8239	0.16 (0.02–1.48)	0.106
Rim	−1.9214	0.15 (0.05–0.42)	<0.001*
Part	0.8467	2.33 (0.84–6.50)	0.105
Whole	1.7276	5.63 (2.61–12.15)	<0.001*
PVP or TP			
Hypointensity	1.8279	6.22 (2.98–12.98)	<0.001*
Others		Reference category	

*$P < 0.05$. HCC, hepatocellular carcinoma; T_2WI, T_2-weighted image; APHE, arterial phase hyperenhancement; PVP, portal venous phase; TP, transitional phase.

Table 3 Multivariate logistic models of Model 2 in Study 1

	Partial regression coefficient	Odds ratio (95% confidence interval)	*P*-value
Step 1: Benign (1) vs. malignant lesions (0)			
(Constant)	–3.3126		
Size	–0.1375	0.87 (0.82–0.93)	<0.001*
T_2WI			
Marked hyperintensity	5.2645	193.34 (47.51–786.86)	<0.001*
Others	Reference category		
T_1WI			
Without signal drop on OP	Reference category		
With signal drop on OP	1.5623	4.77 (0.82–27.79)	0.082
DWI			
Isointensity	Reference category		
Hyperintensity	1.2802	3.60 (0.92–14.14)	0.067
Hypointensity	4.8834	132.07 (12.01–1451.88)	<0.001*
APHE			
Dot-like	3.4136	30.37 (4.02–229.22)	0.001*
Others	Reference category		
HBP			
No uptake of gadoxetate disodium	Reference category		
Marked uptake of gadoxetate disodium	3.8693	47.91 (8.17–280.97)	<0.001*
Moderate uptake of gadoxetate disodium	1.7115	5.54 (0.80–38.09)	0.082
PVP or TP			
Hypointensity	Reference category		
Others	0.8611	2.37 (0.72–7.82)	0.158
Step 2: HCC (1) vs. non-HCC malignant lesions (0)			
(Constant)	–4.7852		
T_2WI			
Iso- or hypointensity	Reference category		
Marked hyperintensity	2.7356	15.42 (1.30–182.20)	0.030*
Hyperintensity	0.9572	2.60 (1.11–6.09)	0.027*
T_1WI			
Without signal drop on OP	Reference category		
With signal drop on OP	1.3777	3.97 (1.03–15.33)	0.046*
APHE			
Dot-like or rim	Reference category		
No	2.1234	8.36 (2.89–24.22)	<0.001*
Part	2.9058	18.28 (5.25–63.59)	<0.001*
Whole	3.9804	53.54 (19.13–149.82)	<0.001*
HBP			
Part uptake of gadoxetate disodium	Reference category		
Whole uptake of gadoxetate disodium	2.3740	10.74 (0.96–119.61)	0.054
No uptake of gadoxetate disodium	0.6253	1.87 (0.63–5.58)	0.262
PVP or TP			
Hypointensity	1.9608	7.11 (2.84–17.78)	<0.001*
Others	Reference category		

*$P < 0.05$. T_2WI, T_2-weighted image; T_1WI, T_1-weighted image; OP, opposed phase; DWI, diffusion-weighted image; APHE, arterial phase hyperenhancement; HBP, hepatobiliary phase; PVP, portal venous phase; TP, transitional phase; HCC, hepatocellular carcinoma.

Table 4 Diagnostic performance of Study 1 [HCC vs. others (benign and non-HCC malignant lesions)]

	Model 1	Model 2
Accuracy (*n*/*n*)	0.835 (313/375)	0.840 (315/375)
Sensitivity (*n*/*n*)	0.879 (175/199)	0.804 (160/199)
Specificity (*n*/*n*)	0.784 (138/176)	0.881 (155/176)
PPV (*n*/*n*)	0.822 (175/213)	0.884 (160/181)
NPV (*n*/*n*)	0.852 (138/162)	0.799 (155/194)
LR+ (95% CI)	4.073 (3.059–5.423)	6.739 (4.485–10.125)
LR– (95% CI)	0.154 (0.105–0.226)	0.223 (0.167–0.296)
AUC (95% CI)	0.903 (0.872–0.933)	N/A

HCC, hepatocellular carcinoma; PPV, positive predictive value; NPV, negative predictive value; LR+, positive likelihood ratio; LR–, negative likelihood ratio; CI, confidence interval; AUC, area under the curve, N/A, not applicable.

Table 5 Diagnostic performance of Model 2 in Study 1

	Benign lesions (*n* = 81) vs. malignant lesions (*n* = 294)	HCC (*n* = 199) vs. non-HCC malignant lesions (*n* = 95)
Accuracy (*n*/*n*)	0.955 (358/375)	0.840 (247/294)
Sensitivity (*n*/*n*)	0.963 (78/81)	0.854 (170/199)
Specificity (*n*/*n*)	0.952 (280/294)	0.811 (77/95)
PPV (*n*/*n*)	0.848 (78/92)	0.904 (170/188)
NPV (*n*/*n*)	0.989 (280/283)	0.726 (77/106)
LR+ (95% CI)	20.231 (12.107–33.776)	4.508 (2.963–6.861)
LR– (95% CI)	0.039 (0.013–0.118)	0.180 (0.127–0.255)
AUC (95% CI)	0.982 (0.970–0.994)	0.880 (0.835–0.926)

HCC, hepatocellular carcinoma; PPV, positive predictive value; NPV, negative predictive value; LR+, positive likelihood ratio; LR–, negative likelihood ratio; AUC, area under the curve; CI, confidence interval.

[range, 8–228] mm; benign lesions, 17.3 ± 21.1 [2–80] mm; and non-HCC malignant lesions including premalignant lesions, 28.0 ± 18.5 [7–73] mm. The mean time interval between gadoxetate disodium-enhanced MRI and pathological diagnosis was 40.7 ± 42.6 days in HCC and 34.0 ± 28.5 days in other lesions. All the images were evaluable for the blind reading. When comparing Study 1's logistic models and MRI decision tree for distinguishing HCC from other lesions to the CT decision tree, the accuracy, sensitivity, negative predictive value, and negative likelihood ratio of the CT decision tree (reader 2) were higher than those of the MRI Model 2 (P = 0.015–0.033) (Table 6). Other diagnostic parameters of the logistic models and MRI decision tree showed no significant differences compared with the CT decision tree (P = 0.059–1.000) (Table 6). Interobserver agreement of the CT and MRI decision trees was good (κ = 0.714 and 0.616) while that of Model 1 and 2 was moderate (κ = 0.415 and 0.452) (Table 6). When compared diagnostic abilities of radiologists-oriented practical diagnosis of CT and MRI, there was no significant difference in any parameters of both readers (P = 0.059–1.000) (Table 7). Interobserver agreement of radiologist-made practical diagnosis of CT and MRI was good (κ = 0.687 and 0.662) (Table 7). The reproducibility of CT and MRI findings between the two readers was moderate or good for all findings (κ = 0.523–0.751) except signal intensity of T_2WI (κ = 0.348). Details of the reproducibility of CT and MRI findings are shown in Table 8. Case examples are shown in Figs. 5 and 6. Figure 5 is a case of cholangiolocellular carcinoma misdiagnosed as HCC on MRI; however, it was correctly diagnosed as "other lesion" on CT. Conversely, Fig. 6 is a case of HCC misdiagnosed as "other lesion" on CT that was correctly diagnosed on MRI.

Discussion

Our study revealed that rim or whole APHE, signal intensities on T_2WI, DWI and PVP/TP/HBP images, and signal drop on opposed-phase images are useful MRI findings for differential diagnosis of HCC. The diagnostic ability of model-based gadoxetate disodium-enhanced MRI for HCC was not superior to that of the CT decision tree—a conventional flowchart for non-invasive diagnosis of HCC. There was no significant difference in radiologist-made practical diagnosis between CT and MRI. Although many sequences can be acquired in gadoxetate disodium-enhanced MRI, only dynamic phases are considered major features in LI-RADS criteria; other findings are listed as ancillary features. Here, we report which MRI findings can be useful for correct diagnosis of HCC. Signal intensity on T_2WI was especially useful for distinguishing HCC from benign and non-HCC malignant lesions, as well as benign lesions from malignant lesions. Signal intensities of DWI and HBP images and pattern of APHE were useful for distinguishing benign lesions from malignant lesions. For differential diagnosis between HCC and non-HCC malignant lesions, signal intensity on T_2WI and pattern of APHE findings can be helpful. However, the reproducibility of signal intensity of T_2WI was lower than that of other MRI and CT findings. These results can be generalized because our study included images from multiple institutions. Whereas, in our study, radiologist-made practical diagnosis showed higher accuracy (0.890) than did the MRI logistic model (0.740–0.810) for reader 2; however, opposite results were obtained for reader 1. It would be interesting to investigate radiologists' imaging findings apart from the features tested in our study to improve the practical diagnostic performance. It shows that diagnostic process for HCC in gadoxetate disodium-enhanced MRI is not one-way pathway and may require individualized decisions tailored to the patient and the clinical context.[6]

Although gadoxetate disodium is widely used for liver MRI,7–9 previous studies with pathologically proven HCCs or HCCs of size >1 cm showed that the diagnostic ability of gadoxetate disodium-enhanced MRI is not necessarily higher

Table 6 Results of Study 2 by decision tree and logistic model [HCC vs. others (benign and non-HCC malignant lesions)]

		CT decision tree	MRI decision tree	*P*-value (vs. CT)	MRI Model 1	*P*-value (vs. CT)	MRI Model 2	*P*-value (vs. CT)
Accuracy (*n*/*n*)	Reader 1	0.850 (85/100)	0.850 (85/100)	1.000	0.860 (86/100)	1.000	0.820 (82/100)	0.663
	Reader 2	0.860 (86/100)	0.810 (81/100)	0.383	0.780 (78/100)	0.153	0.740 (74/100)	0.031*
Sensitivity (*n*/*n*)	Reader 1	0.877 (64/73)	0.918 (67/73)	0.366	0.959 (70/73)	0.083	0.904 (66/73)	0.593
	Reader 2	0.945 (69/73)	0.890 (65/73)	0.248	0.904 (66/73)	0.366	0.836 (61/73)	0.033*
Specificity (*n*/*n*)	Reader 1	0.778 (21/27)	0.667 (18/27)	0.257	0.593 (16/27)	0.059	0.593 (16/27)	0.059
	Reader 2	0.630 (17/27)	0.593 (16/27)	0.739	0.444 (12/27)	0.166	0.481 (13/27)	0.248
PPV (*n*/*n*)	Reader 1	0.914 (64/70)	0.882 (67/76)	0.320	0.864 (70/81)	0.113	0.857 (66/77)	0.078
	Reader 2	0.873 (69/79)	0.855 (65/76)	0.594	0.815 (66/81)	0.129	0.813 (61/75)	0.121
NPV (*n*/*n*)	Reader 1	0.700 (21/30)	0.750 (18/27)	0.592	0.842 (16/19)	0.208	0.696 (16/23)	0.967
	Reader 2	0.810 (17/21)	0.667 (16/24)	0.229	0.632 (12/19)	0.172	0.520 (13/25)	0.015*
LR+ (95% CI)	Reader 1	3.945 (1.938–8.032)	2.753 (1.608–4.715)	0.323	2.354 (1.490–3.719)	0.117	2.219 (1.400–3.519)	0.082
	Reader 2	2.552 (1.557–4.186)	2.186 (1.377–3.469)	0.594	1.627 (1.152–2.299)	0.132	1.612 (1.105–2.351)	0.123
LR– (95% CI)	Reader 1	0.159 (0.083–0.302)	0.123 (0.055–0.278)	0.594	0.069 (0.022–0.219)	0.226	0.162 (0.075–0.350)	0.967
	Reader 2	0.087 (0.032–0.236)	0.185 (0.090–0.382)	0.238	0.216 (0.095–0.490)	0.179	0.341 (0.178–0.653)	0.020*
Kappa value		0.714 (0.557–0.870)	0.616 (0.432–0.801)	—	0.415 (0.188–0.642)	—	0.452 (0.246–0.658)	—

*$P < 0.05$. HCC, hepatocellular carcinoma; CT, computed tomography; MRI, magnetic resonance imaging; PPV, positive predictive value; NPV, negative predictive value; LR+, positive likelihood ratio; LR–, negative likelihood ratio; CI, confidence interval.

Table 7 Diagnostic performance of Study 2 by radiologist-made practical diagnosis [HCC vs. others (benign and non-HCC malignant lesions)]

		CT	MRI	*P*-value
AUC (95% CI)	Reader 1	0.865 (0.775–0.955)	0.799 (0.694–0.904)	0.169
	Reader 2	0.867 (0.777–0.958)	0.866 (0.779–0.952)	0.976
Accuracy (*n*/*n*)	Reader 1	0.869 (86/99)	0.818 (81/99)	0.267
	Reader 2	0.890 (89/100)	0.890 (89/100)	1.000
Sensitivity (*n*/*n*)	Reader 1	0.917 (66/72)	0.918 (67/73)	1.000
	Reader 2	0.932 (68/73)	0.959 (70/73)	0.414
Specificity (*n*/*n*)	Reader 1	0.741 (20/27)	0.538 (14/26)	0.059
	Reader 2	0.778 (21/27)	0.704 (19/27)	0.414
PPV (*n*/*n*)	Reader 1	0.904 (66/73)	0.848 (67/79)	0.061
	Reader 2	0.919 (68/74)	0.897 (70/78)	0.465
NPV (*n*/*n*)	Reader 1	0.769 (20/26)	0.700 (14/20)	0.487
	Reader 2	0.808 (21/26)	0.864 (19/22)	0.520
LR+ (95% CI)	Reader 1	3.536 (1.862–6.715)	1.989 (1.306–3.029)	0.064
	Reader 2	4.192 (2.064–8.512)	3.236 (1.806–5.799)	0.467
LR– (95% CI)	Reader 1	0.113 (0.051–0.250)	0.153 (0.066–0.355)	0.487
	Reader 2	0.088 (0.037–0.210)	0.058 (0.019–0.182)	0.524
Kappa value		0.687 (0.521–0.853)	0.662 (0.475–0.848)	—

HCC, hepatocellular carcinoma; CT, computed tomography; MRI, magnetic resonance imaging; AUC, area under the curve; CI, confidence interval; PPV, positive predictive value; NPV, negative predictive value; LR+, positive likelihood ratio; LR–, negative likelihood ratio.

Table 8 Reproducibility of MRI and CT findings between the two readers in Study 2

	Reader 1	Reader 2	κ-value (95% confidence interval)
MRI findings			
SI of T_2WI (hypo/iso/hyper/marked hyper)	0/16/74/10	0/5/92/3	0.348 (0.147–0.550)
Signal drop on OP (yes/no)	23/77	25/75	0.562 (0.369–0.755)
SI of DWI (hypo/iso/hyper)	0/28/72	3/12/85	0.523 (0.325–0.721)
Pattern of APHE (no/dot-like/rim/part/whole)	18/3/2/20/57	16/2/10/22/50	0.664 (0.491–0.838)
SI of PVP (marked hypo/hypo/iso/hyper)	77/1/14/8	74/5/10/11	0.645 (0.461–0.829)
SI of TP (marked hypo/hypo/iso/hyper)	82/1/12/5	80/5/9/6	0.584 (0.365–0.803)
Uptake of gadoxetate disodium on HBP (no/part and moderate/part and marked/whole and moderate/whole and marked)	86/6/3/3/2	73/20/0/4/3	0.659 (0.393–0.926)
CT findings			
Non-rim APHE (yes/no)	84/16	92/8	0.534 (0.284–0.784)
Non-peripheral washout (yes/no)	73/27	80/20	0.751 (0.598–0.905)

MRI, magnetic resonance imaging; CT, computed tomography; SI, signal intensity; T_2WI, T_2-weighted image; OP, opposed phase; DWI, diffusion-weighted image; APHE, arterial phase hyperenhancement; PVP, portal venous phase; TP, transitional phase; HBP, hepatobiliary phase; AP, arterial phase.

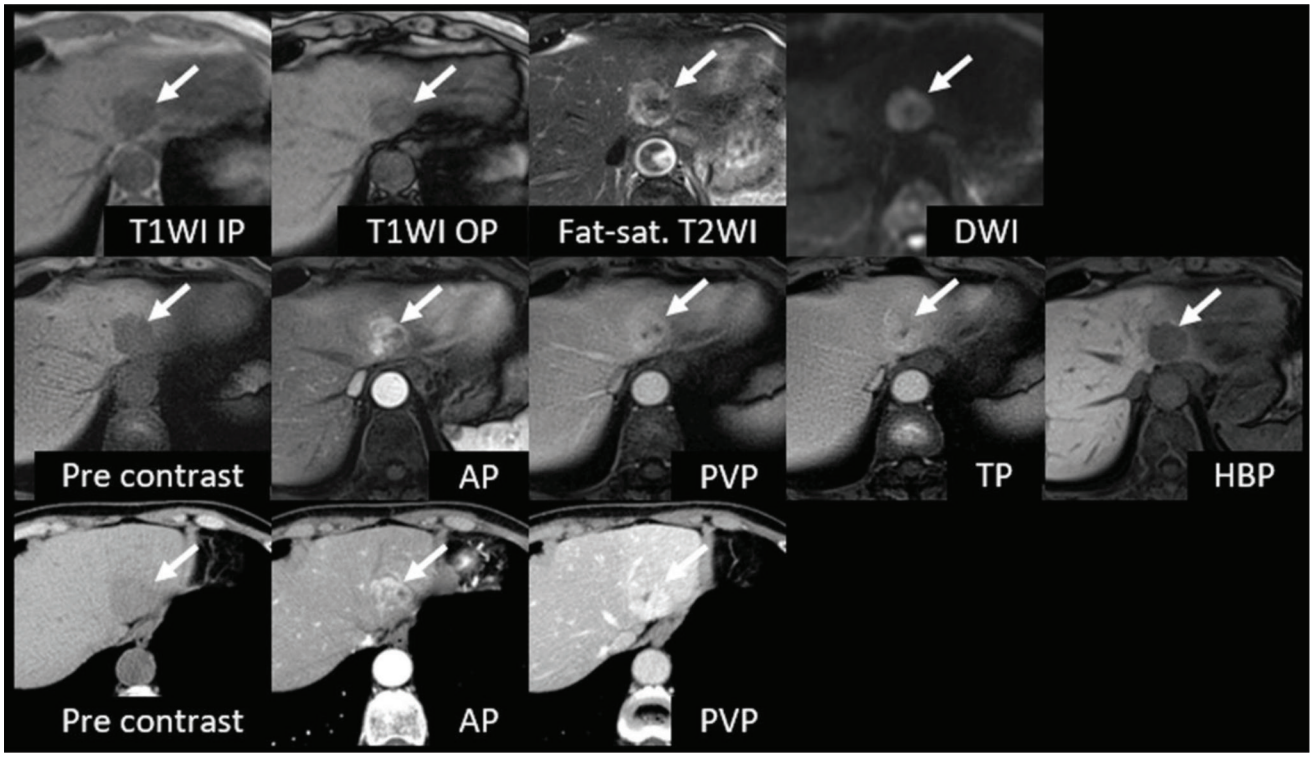

Fig. 5 A case of cholangiolocellular carcinoma (CoCC) misdiagnosed as hepatocellular carcinoma (HCC) on magnetic resonance imaging (MRI). The top and middle rows show MR images and the bottom row shows computed tomography (CT) images. A 78-year-old woman had CoCC (24 mm) at S2 (arrows). This lesion did not show marked hyperintensity on T_2-weighted images (T_2WI). Non-rim arterial phase hyperenhancement (APHE) was shown on both CT and MRI. Signal drop of opposed phase (OP) and gadoxetic acid uptake at the hepatobiliary phase (HBP) were not observed. Portal venous phase (PVP) and transitional phase (TP) images on MRI showed hyperintensity. This lesion was misdiagnosed as HCC by the logistic model, decision tree of MRI, and radiologist-made practical diagnosis of MRI (both readers scored 5 for both malignancy and HCC). On CT, this lesion was correctly diagnosed as "other lesion" (a category that includes benign and non-HCC malignant lesions) by the decision tree and radiologist-made practical diagnosis (reader 1 scored 2 for malignancy while reader 2 scored 5 for malignancy and 2 for HCC) because non-peripheral washout was not observed. T_1WI, T_1-weighted image; IP, in phase; Fat-sat., fat-saturated; DWI, diffusion-weighted image.

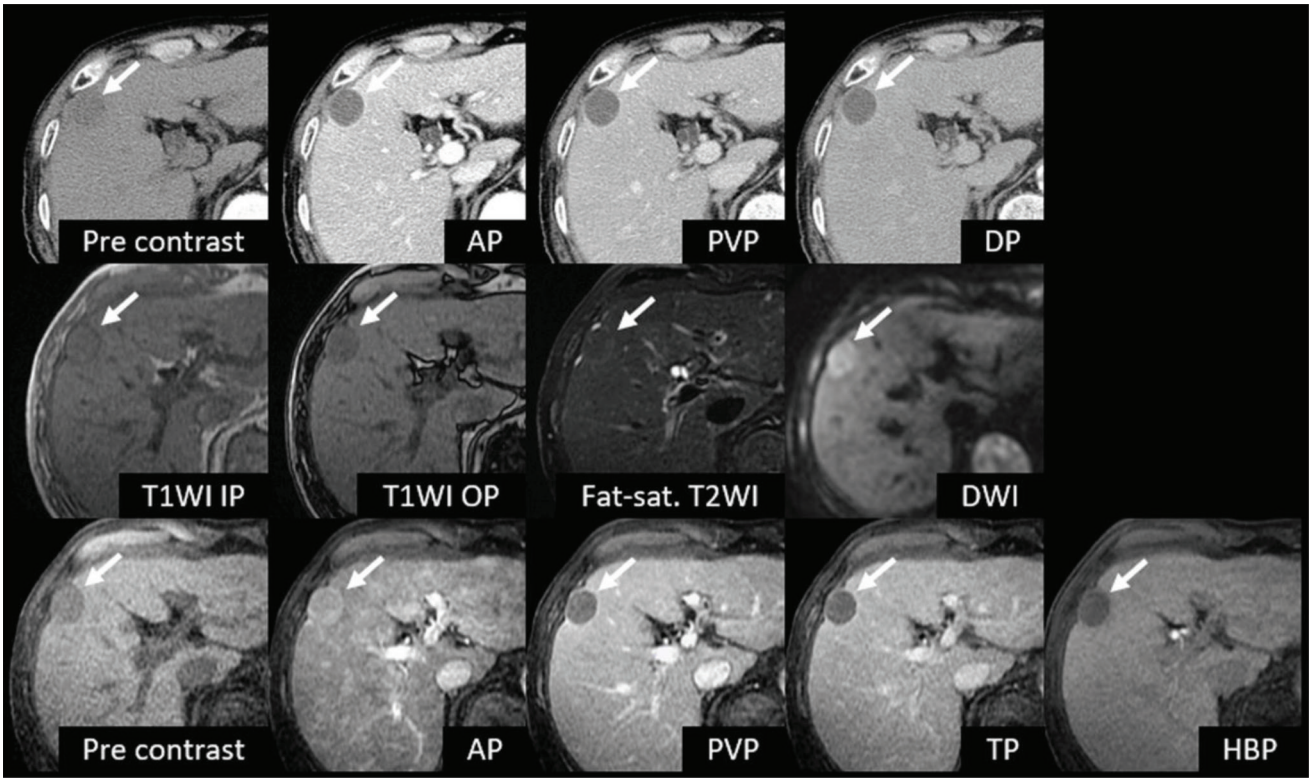

Fig. 6 A case of hepatocellular carcinoma (HCC) misdiagnosed as "other lesion" (a category that includes benign and non-HCC malignant lesions) on computed tomography (CT) while correctly diagnosed on magnetic resonance imaging (MRI). The top row shows CT images and the middle and bottom rows show MR images. A 73-year-old man had HCC (22 mm) at S5 (arrows). This lesion showed rim arterial phase hyperenhancement (APHE) on CT. Therefore, it was misdiagnosed as "other lesion" (benign and non-HCC malignant lesions) by the decision tree and radiologist-made practical diagnosis (reader 1 scored 2 and reader 2 scored 3 for malignancy). On MRI, this lesion did not show marked hyperintensity on T_2-weighted images (T_2WI). Non-rim APHE and signal drop of opposed phase (OP) were observed. Gadoxetic acid uptake on hepatobiliary phase (HBP) was not observed. Portal venous phase (PVP) and transitional phase (TP) images on MRI showed hypointensity. This lesion was correctly diagnosed as HCC by the logistic model, decision tree of MRI, and radiologist-made practical diagnosis of MRI (both readers scored 5 for both malignancy and HCC). T_1WI, T_1-weighted image; IP, in phase; Fat-sat., fat-saturated; DWI, diffusion-weighted image.

than that of dynamic CT.[22–24] The advantages of gadoxetate disodium-enhanced MRI are linked to the HBP, which can detect small HCCs; distinguish HCCs from hypervascular pseudolesions; and discover HBP hypointense nodules without APHE and early HCC or a premalignant lesion that is expected to become a typical HCC over time.[10,22–28] In our study, the diagnostic performance of gadoxetate disodium-enhanced MRI was not superior to that of dynamic CT, as only 11% (11/100) of the lesions in Study 2 were small (<1 cm). Additionally, only one HBP hypointense nodule without APHE was included and was not targeted as an endpoint. Nonetheless, we believe that our results do not deny the utility of gadoxetate disodium-enhanced MRI for management of patients with cirrhosis/HCC. More studies are necessary to investigate the advantages of gadoxetate disodium-enhanced MRI over dynamic CT. In general, specificity is important for diagnosis of HCC. However, the specificity of gadoxetate disodium-enhanced MRI in our study was relatively low for both readers (0.444–0.667) compared with that in previous reports (~0.9).[22,23,25] This was because of differences in target cases: our study included many mimickers of HCC, such as intrahepatic cholangiocarcinoma, cholangiolocellular carcinoma, neuroendocrine tumor, and hypervascular pseudolesion, which can be misdiagnosed as HCC because of non-rim APHE[29–32] and hypointensity on HBP.[33] According to the Liver Cancer Study Group of Japan registry data in 2006–2007, the ratio of intrahepatic cholangiocarcinoma vs. HCC was 208:15250 (≈1:73) in patients with chronic liver disease.[34] Our study population tended toward non-HCC malignancy (intrahepatic cholangiocarcinoma and combined hepatocellular-cholangiocarcinoma) (non-HCC malignant lesions [n = 12] vs. HCC [n = 73] ≈ 1:6). Therefore, the distributions of HCC and non-HCC did not represent the natural population, although the data were prospectively collected in Study 2. The positive predictive value of gadoxetate disodium-enhanced MRI could be sufficiently high within our results, if the incidence rates of HCC and non-HCC were considered.

Our study has some limitations. First, although we enrolled patients prospectively in Study 2, the ratio of HCC and non-HCC lesions was different from that of the general

population. We were unable to calculate accurate positive/negative predictive values. Second, our study cohort of 100 lesions in Study 2 was relatively small in terms of sample size. However, we discontinued enrollment because reasonable statistical power was expected with this number of cases. Third, we evaluated the diagnostic ability of CT and gadoxetate disodium-enhanced MRI for HCC in patients with relatively good liver function who could undergo surgery or biopsy, rather than of patients with advanced or end-stage cirrhosis and HCC. This could have influenced the diagnostic ability of gadoxetate disodium-enhanced MRI. Fourth, the MRI and CT parameters were not necessarily were not along with LI-RADS recommendation because the imaging studies were performed as part of each hospital's daily practice.

Conclusion

In summary, we show an MRI decision tree and logistic models for HCC diagnosis. A combination of gadoxetate disodium-enhanced MRI findings was useful for HCC diagnosis. However, its diagnostic ability was not superior to that of dynamic CT. Further studies warranted to further define the role of gadoxetate disodium-enhanced MRI in patients with chronic liver disease because the ratio of HCC and non-HCC lesions was different from that of the general population in our study cohort.

Acknowledgments

We thank the participants in this multicenter trial, who were selected from the radiology departments of the following institutions: Tokyo Medical University, Tokai University Hachioji Hospital, Niigata University, Shinshu University, Fujita Health University, Hamamatsu University School of Medicine, Kanazawa University, Nara Medical University, Yamaguchi University, Nagasaki University, and Kagoshima University. We also thank Mr. M. Fuchigami from Kondo Photo Process Co., Ltd. for statistical analysis.

Conflicts of Interest

This project was supported by Bayer Yakuhin, Ltd. There are no other conflicts of interest to declare.

Appendix: Method for Determining Lesions in Logistic Model

Model 1 [HCC vs. others (benign and non-HCC malignant lesions)]

logit P = –3.9855 + 1.8279 × hypointensity on PVP or TP [0, 1] – 1.8239 × dot-like APHE [0, 1] – 1.9214 × rim APHE [0, 1] + 0.8467 × part APHE [0, 1] + 1.7276 × whole APHE [0, 1] + 2.2667 × hyperitensity on T_2WI [0, 1] + 2.0302 × isointensity on T_2WI [0, 1] – 13.4752 × hypointensity on T_2WI [0, 1] + 0.0197 × size (mm)

If $P \geq 0.5150$, the lesion was judged as HCC.

Model 2 (benign vs. malignant lesions)

logit P = –3.3126 + 0.1375 × size (mm) + 5.2645 ≠ marked hyperitensity on T_2WI [0, 1] + 1.5623 × signal drop on OP [0, 1] + 1.2802 × hyperitensity on DWI [0, 1] + 4.8834 × hypointensity on DWI [0, 1] + 3.4136 × dot-like APHE [0,1] + 3.8693 × marked uptake of gadoxeate disodium on HBP [0, 1] × moderate uptake gadoxate disodium on HBP [0, 1] + 0.8611 × except for Hypointensity on PVP and TP [0, 1]

If $P \geq 0.1871$, the lesion was judged as benign lesions.

Model 2 (HCC vs. non-HCC malignant lesions)

logit P = –4.7852 + 2.7356 × marked hyperintensity on T_2WI [0, 1] + 0.9572 × hyperintensity on T_2WI [0, 1] + 1.3777 × signal drop on OP [0, 1] + 2.1234 × no APHE [0, 1] + 2.9058 × part APHE [0, 1] + 3.9804 × whole APHE [0, 1] + 2.3740 × whole uptake of gadoxetate disodium on HBP [0, 1] + 0.6253 × no uptake of gadoxetate disodium on HBP [0, 1] + 1.9608 × hypointensity on PVP or TP [0, 1]

If $P \geq 0.6774$, the lesion was judged as benign lesions.

In those equations, if applicable, 1 was assigned and if not applicable, 0 was assigned to the category variable.

References

1. Ferlay J, Colombet M, Soerjomataram I, et al. Estimating the global cancer incidence and mortality in 2018: GLOBOCAN sources and methods. Int J Cancer 2019; 144:1941–1953.
2. Beal EW, Tumin D, Kabir A, et al. Trends in the mortality of hepatocellular carcinoma in the United States. J Gastrointest Surg 2017; 21:2033–2038.
3. Ascione A, Fontanella L, Imparato M, Rinaldi L, De Luca M. Mortality from cirrhosis and hepatocellular carcinoma in Western Europe over the last 40 years. Liver Int 2017; 37:1193–1201.
4. Zhu RX, Seto WK, Lai CL, Yuen MF. Epidemiology of hepatocellular carcinoma in the Asia-Pacific region. Gut Liver 2016; 10:332–339.
5. Marrero JA, Kulik LM, Sirlin CB, et al. Diagnosis, staging, and management of hepatocellular carcinoma: 2018 practice guidance by the American Association for the Study of Liver Diseases. Hepatology 2018; 68:723–750.
6. American College of Radiology. CT/MRI LI-RADS® v2018. 2018. Available at: https://www.acr.org/Clinical-Resources/Reporting-and-Data-Systems/LI-RADS/CT-MRI-LI-RADS-v2018.
7. Moon JY, Kim SH, Choi SY, Hwang JA, Lee JE, Lee J. Differentiating malignant from benign hyperintense nodules on unenhanced T1-weighted images in patients with chronic liver disease: using gadoxetic acid-enhanced and diffusion-weighted MR imaging. Jpn J Radiol 2018; 36:489–499.

8. Asato N, Tsurusaki M, Sofue K, et al. Comparison of gadoxetic acid-enhanced dynamic MR imaging and contrast-enhanced computed tomography for preoperative evaluation of colorectal liver metastases. Jpn J Radiol 2017; 35:197–205.
9. Chen N, Motosugi U, Morisaka H, et al. Added value of a gadoxetic acid-enhanced hepatocyte-phase image to the LI-RADS system for diagnosing hepatocellular carcinoma. Magn Reson Med Sci 2016; 15:49–59.
10. Tsurusaki M, Sofue K, Isoda H, Okada M, Kitajima K, Murakami T. Comparison of gadoxetic acid-enhanced magnetic resonance imaging and contrast-enhanced computed tomography with histopathological examinations for the identification of hepatocellular carcinoma: a multicenter phase III study. J Gastroenterol 2016; 51:71–79.
11. Yoon JH, Lee JM, Lee YJ, Lee KB, Han JK. Added value of sequentially performed gadoxetic acid-enhanced liver MRI for the diagnosis of small (10-19 mm) or atypical hepatic observations at contrast-enhanced CT: a prospective comparison. J Magn Reson Imaging 2019; 49:574–587.
12. Liu X, Jiang H, Chen J, Zhou Y, Huang Z, Song B. Gadoxetic acid disodium-enhanced magnetic resonance imaging outperformed multidetector computed tomography in diagnosing small hepatocellular carcinoma: a meta-analysis. Liver Transpl 2017; 23:1505–1518.
13. Motosugi U, Bannas P, Bookwalter CA, Sano K, Reeder SB. An investigation of transient severe motion related to gadoxetic acid-enhanced MR imaging. Radiology 2016; 279:93–102.
14. McClellan TR, Motosugi U, Middleton MS, et al. Intravenous gadoxetate disodium administration reduces breath-holding capacity in the hepatic arterial phase: a multi-center randomized placebo-controlled trial. Radiology 2017; 282:361–368.
15. Motosugi U, Ichikawa T, Sou H, et al. Dilution method of gadolinium ethoxybenzyl diethylenetriaminepentaacetic acid (Gd-EOB-DTPA)-enhanced magnetic resonance imaging (MRI). J Magn Reson Imaging 2009; 30:849–854.
16. Ichikawa S, Motosugi U, Oishi N, et al. Ring-like enhancement of hepatocellular carcinoma in gadoxetic acid-enhanced multiphasic hepatic arterial phase imaging with differential subsampling with cartesian ordering. Invest Radiol 2018; 53:191–199.
17. Kitao A, Matsui O, Yoneda N, et al. Hypervascular hepatocellular carcinoma: correlation between biologic features and signal intensity on gadoxetic acid-enhanced MR images. Radiology 2012; 265:780–789.
18. Kitao A, Matsui O, Yoneda N, et al. Hepatocellular carcinoma with β-catenin mutation: imaging and pathologic characteristics. Radiology 2015; 275:708–717.
19. Motosugi U, Murakami T, Lee JM, et al. Recommendation for terminology: nodules without arterial phase hyperenhancement and with hepatobiliary phase hypointensity in chronic liver disease. J Magn Reson Imaging 2018; 48:1169–1171.
20. Bruix J, Sherman M; American Association for the Study of Liver Diseases. Management of hepatocellular carcinoma: an update. Hepatology 2011; 53:1020–1022.
21. Breiman L, Friedman J, Olshen R, Stone C. Classification and regression trees. Wadsworth International Group, Belmont, CA, 1984.
22. Kakihara D, Nishie A, Harada N, et al. Performance of gadoxetic acid-enhanced MRI for detecting hepatocellular carcinoma in recipients of living-related-liver-transplantation: comparison with dynamic multidetector row computed tomography and angiography-assisted computed tomography. J Magn Reson Imaging 2014; 40:1112–1120.
23. Kim SH, Kim SH, Lee J, et al. Gadoxetic acid-enhanced MRI versus triple-phase MDCT for the preoperative detection of hepatocellular carcinoma. AJR Am J Roentgenol 2009; 192:1675–1681.
24. Kim YK, Kim CS, Han YM, et al. Detection of hepatocellular carcinoma: gadoxetic acid-enhanced 3-dimensional magnetic resonance imaging versus multi-detector row computed tomography. J Comput Assist Tomogr 2009; 33: 844–850.
25. Di Martino M, De Filippis G, De Santis A, et al. Hepatocellular carcinoma in cirrhotic patients: prospective comparison of US, CT and MR imaging. Eur Radiol 2013; 23:887–896.
26. Kim SE, Lee HC, Shim JH, et al. Noninvasive diagnostic criteria for hepatocellular carcinoma in hepatic masses >2 cm in a hepatitis B virus-endemic area. Liver Int 2011; 31:1468–1476.
27. Guo J, Seo Y, Ren S, et al. Diagnostic performance of contrast-enhanced multidetector computed tomography and gadoxetic acid disodium-enhanced magnetic resonance imaging in detecting hepatocellular carcinoma: direct comparison and a meta-analysis. Abdom Radiol (NY) 2016; 41:1960–1972.
28. Ichikawa T, Sano K, Morisaka H. Diagnosis of pathologically early HCC with EOB-MRI: experiences and current consensus. Liver Cancer 2014; 3:97–107.
29. Choi SH, Lee SS, Kim SY, et al. Intrahepatic cholangiocarcinoma in patients with cirrhosis: differentiation from hepatocellular carcinoma by using gadoxetic acid-enhanced MR imaging and dynamic CT. Radiology 2017; 282:771–781.
30. Kim R, Lee JM, Shin CI, et al. Differentiation of intrahepatic mass-forming cholangiocarcinoma from hepatocellular carcinoma on gadoxetic acid-enhanced liver MR imaging. Eur Radiol 2016; 26:1808–1817.
31. Haradome H, Unno T, Morisaka H, et al. Gadoxetic acid disodium-enhanced MR imaging of cholangiolocellular carcinoma of the liver: imaging characteristics and histopathological correlations. Eur Radiol 2017; 27:4461–4471.
32. Cha DI, Kang TW, Jang KM, et al. Hepatic neuroendocrine tumors: gadoxetic acid-enhanced magnetic resonance imaging findings with an emphasis on differentiation between primary and secondary tumors. Abdom Radiol (NY) 2018; 43:3331–3339.
33. Motosugi U, Ichikawa T, Sou H, et al. Distinguishing hypervascular pseudolesions of the liver from hypervascular hepatocellular carcinomas with gadoxetic acid-enhanced MR imaging. Radiology 2010; 256:151–158.
34. Kudo M, Izumi N, Ichida T, et al. Report of the 19th follow-up survey of primary liver cancer in Japan. Hepatol Res 2016; 46:372–390.